Inorganic Chemistry

Article

pubs.acs.org/IC

Effect of Lone-Electron-Pair Cations on the Orientation of Crystallographic Shear Planes in Anion-Deficient Perovskites

Dmitry Batuk,*[†] Maria Batuk,[†] Artem M. Abakumov,[†] Alexander A. Tsirlin,[‡,§] Catherine McCammon,[⊥] Leonid Dubrovinsky,[⊥] and Joke Hadermann[†]

[†]Electron Microscopy for Materials Research (EMAT), University of Antwerp, Groenenborgerlaan 171, B-2020 Antwerp, Belgium
[‡]National Institute of Chemical Physics and Biophysics, 12618 Tallinn, Estonia
[§]Max Planck Institute for Chemical Physics of Solids, Nöthnitzer Strasse 40, 01187 Dresden, Germany
[⊥]Bayerisches Geoinstitut, Universität Bayreuth, 95440 Bayreuth, Germany

Ⓢ *Supporting Information*

ABSTRACT: Factors affecting the structure and orientation of the crystallographic shear (CS) planes in anion-deficient perovskites were investigated using the $(Pb_{1-z}Sr_z)_{1-x}Fe_{1+x}O_{3-y}$ perovskites as a model system. The isovalent substitution of Sr^{2+} for Pb^{2+} highlights the influence of the A cation electronic structure because these cations exhibit very close ionic radii. Two compositional ranges have been identified in the system: $0.05 \leq z \leq 0.2$, where the CS plane orientation gradually varies but stays close to $(203)_p$, and $0.3 \leq z \leq 0.45$ with $(101)_p$ CS planes. The incommensurately modulated structure of $Pb_{0.792}Sr_{0.168}Fe_{1.040}O_{2.529}$ was refined from neutron powder diffraction data using the (3 + 1)D approach (space group $X2/m(\alpha0\gamma)$, $X = (^1/_2, ^1/_2, ^1/_2, ^1/_2)$, $a = 3.9512(1)$ Å, $b = 3.9483(1)$ Å, $c = 3.9165(1)$ Å, $\beta = 93.268(2)°$, $\mathbf{q} = 0.0879(1)\mathbf{a}^* + 0.1276(1)\mathbf{c}^*$, $R_F = 0.023$, $R_P = 0.029$, and $T = 900$ K). A comparison of the compounds with different CS planes indicates that the orientation of the CS planes is governed mainly by the stereochemical activity of the lone-electron-pair cations inside the perovskite blocks.

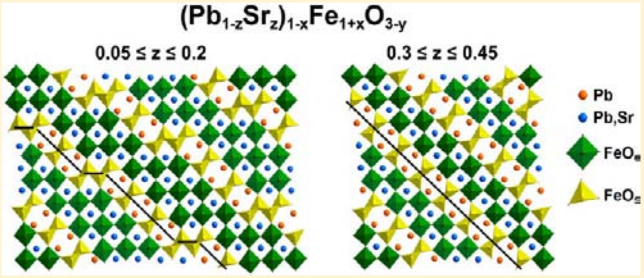

■ INTRODUCTION

The formation of crystallographic shear (CS) planes is a well-known mechanism of the anion deficiency accommodation in oxides with ReO_3 (e.g., WO_3, NbO_2F) and rutile (e.g., TiO_2, VO_2) structures.[1−3] Both structure types are composed of MO_6 octahedra bound in a 3D framework by sharing vertexes (ReO_3) or vertexes and edges (rutile). The anion deficiency in these materials can be introduced either by reduction of the metal cation or by substitution with other cations having lower oxidation state (e.g., W^{6+} and Mo^{6+} by Ti^{4+}, Ge^{4+}, Nb^{5+}, and Ta^{5+}).[4−7] Either way, the overall oxygen content is decreased through CS plane formation. The CS operation can be represented with the following virtual steps: (1) cutting the basic structure along a certain crystallographic plane; (2) removing part of the O atoms along the cut; (3) closing the gap by shifting one part of the structure with respect to another over the displacement vector, which is a fraction of the lattice translation.[3] Typically, the CS operation does not alter the cation coordination number but lowers the oxygen content through a change in the connectivity of the MO_6 octahedra. It introduces edge and face sharing into the ReO_3 and rutile-type structures, respectively.

Upon reduction of the oxygen content, the number of CS planes increases and the distance between them becomes shorter. In some cases, the increasing interaction between the CS planes can force them into ordered arrays, thus giving rise to homologous series, e.g., Ti_nO_{2n-1},[8] V_nO_{2n-1},[9] $(W,Mo)_nO_{3n-1}$, and W_nO_{3n-2}[10,11] (n represents the number of octahedra between the CS planes). Not only the spacing between the CS planes but also their crystallographic orientation depend on the reduction rate. For example, in slightly reduced $WO_{3-\delta}$, down to a composition of about $WO_{2.97}$, the CS planes are confined to the {102} planes (the plane indexes are represented according to the basic cubic ReO_3-type structure). Below a composition of approximately $WO_{2.93}$, they exhibit {103} orientation. At intermediate compositions, the {102} and {103} CS planes coexist.[1] A similar behavior of the CS planes is observed when the oxygen content in WO_3 is reduced by replacing a small amount of W^{6+} by other cations with lower valence state.[4−7] Starting from the low-index {102} planes, upon reduction of the oxygen content, the CS planes subsequently change their orientation toward high-index {103}, {104}, and {10m} planes and ultimately end up with {10∞}, which is equivalent to {001}. In ref 12, such behavior was explained in a semiquantitative manner by the interplay of the CS plane formation energy and the energy of their interaction. The former term is mainly due to rupture of the

Received: May 24, 2013
Published: August 22, 2013

dx.doi.org/10.1021/ic4012845 | *Inorg. Chem.* 2013, 52, 10009−10020

Table 1. Composition, Unit Cell Parameters, Unit Cell Volume, and the Modulation Vector Components of the $(Pb_{1-z}Sr_z)_{1-x}Fe_{1+x}O_{3-y}$ ($0.05 \leq z \leq 0.2$) Compounds, the Interplanar Spacing between the CS Planes (d), and the Average Number of the Octahedra between the Adjacent CS Planes (N)

		cell parameters					modulation vector			
composition	z	a, Å	b, Å	c, Å	β, deg	V, Å^3	α	γ	d,[a] Å	N[b]
$Pb_{0.904}Sr_{0.048}Fe_{1.049}O_{2.535}$	0.05	3.9166(1)	3.8996(1)	3.9249(1)	93.039(1)	59.861(3)	0.0797(1)	0.1283(1)	12.67	3.20
$Pb_{0.859}Sr_{0.095}Fe_{1.046}O_{2.533}$	0.10	3.9170(1)	3.9052(1)	3.9080(1)	93.076(1)	59.692(2)	0.0823(1)	0.1283(1)	12.51	3.09
$Pb_{0.837}Sr_{0.120}Fe_{1.044}O_{2.530}$	0.125	3.9174(1)	3.9077(1)	3.8948(1)	93.122(1)	59.542(3)	0.0846(1)	0.1286(1)	12.35	3.00
$Pb_{0.813}Sr_{0.144}Fe_{1.043}O_{2.528}$	0.15	3.9178(1)	3.9096(1)	3.8881(1)	93.142(1)	59.464(3)	0.0857(1)	0.1287(1)	12.28	2.95
$Pb_{0.792}Sr_{0.168}Fe_{1.040}O_{2.529}$	0.175	3.9184(1)	3.9109(1)	3.8818(1)	93.200(1)	59.393(4)	0.0879(1)	0.1280(1)	12.21	2.89
$Pb_{0.768}Sr_{0.192}Fe_{1.040}O_{2.525}$	0.20	3.9192(1)	3.9123(1)	3.8796(1)	93.210(2)	59.393(4)	0.0885(2)	0.1287(1)	12.13	2.85

[a] $d = 1/2[(\alpha^2/(a^2 \sin^2 \beta) + \gamma^2/(c^2 \sin^2 \beta) - (2\alpha\gamma \cos \beta)/(ac \sin^2 \beta)]^{-1/2}$ [b] $N = (1 - 3\gamma - \alpha)/[2\alpha(2 + \gamma - \alpha)]$.

W–O bonds. In a given structure, the formation energy increases with increasing m of the $\{10m\}$ CS planes. The latter energy term is mainly due to the strain imposed by the CS planes. It depends on the distance between the CS planes, but in general it decreases with increasing m.[13,14] Upon reduction, this term becomes more important and evokes the transition to higher-index $\{10m\}$ CS planes.

Although the structure of perovskites ABO_3 is based on the framework of corner-sharing BO_6 octahedra, similar to that of ReO_3, CS structures in perovskites are not common. The presence of the A cations in cuboctahedral cavities of the perovskite framework prevents a direct application of the CS operation, which makes point vacancies a more favorable mechanism of the anion deficiency accommodation.[15] The formation of CS planes in the perovskite structure requires a substantial rearrangement of the coordination environment of both the A and B cations.[16,17] Thus, at the CS planes, the corner-sharing BO_6 octahedra transform into edge-sharing distorted BO_5 square pyramids. Together with the octahedra from the perovskite blocks, they form a very asymmetric coordination environment for the A positions, which can be occupied by the lone-electron-pair cations (Pb^{2+} and Bi^{3+}) only.

A remarkable example of a perovskite-based system with the CS structure is given by the $(Pb,Bi)_{1-x}Fe_{1+x}O_{3-y}$ series. These compounds are built of the perovskite blocks separated by the equally spaced CS planes with an orientation of approximately $(509)_p$ (the subscript "p" refers to perovskite subcell).[18] In both limiting compounds "$Pb_2Fe_2O_5$" and $BiFeO_3$, the oxidation state of iron is 3+.[19,20] The oxygen content in the series is varied through changes of the Pb^{2+}/Bi^{3+} ratio. It affects only the thickness of the perovskite blocks, whereas the orientation of the CS planes almost does not change. This behavior differs from that of the CS planes in the WO_3-based structures, where the orientation of the planes depends on the degree of reduction. In perovskites, the orientation of the CS planes is altered when the lone-electron-pair cations Pb^{2+} and Bi^{3+} are partially substituted by alkali-earth cations (Ba^{2+} or Sr^{2+}) occupying the A position of the perovskite blocks between the CS planes. Such a replacement stabilizes the $(101)_p$ CS planes and results in the $A_nB_nO_{3n-2}$ perovskite-based homologous series.[21,22] In the original papers, the orientation of these CS planes is defined as $(1\bar{0}1)_p$; however for consistency of the data representation, in this contribution they will be defined as $(101)_p$. These options are interchangeable; the difference is attributed to a slightly different choice of the perovskite sublattice.

To elucidate the effect of the A cation on the behavior of the CS planes in perovskites, we studied the replacement of Pb^{2+} by Sr^{2+} in the $(Pb_{1-z}Sr_z)_{1-x}Fe_{1+x}O_{3-y}$ ferrites. The Pb^{2+} and Sr^{2+} cations exhibit the same oxidation state and similar ionic radii [$r(Pb^{2+})_{XII}$ = 1.49 Å; $r(Sr^{2+})_{XII}$ = 1.44 Å].[23] Therefore, this substitution highlights the effect of an A cation electronic configuration (i.e., the presence or absence of the lone electron pair) on the orientation of the CS planes in perovskites. In this contribution, we demonstrate that variation of the CS plane orientation is related to the stereochemical activity of the lone-electron-pair A cations.

EXPERIMENTAL SECTION

A preliminary investigation of Pb^{2+} substitution with Sr^{2+} in "$Pb_2Fe_2O_5$" was conducted on samples with the general formula $(Pb_{1-z}Sr_z)_2Fe_2O_5$. Several compositional ranges comprising the perovskite-based compounds with different orientations of the CS planes were identified. Then, the single-phase samples from these compositional ranges were prepared and characterized (see Tables 1 and 4). All samples of lead–strontium ferrites were synthesized by a solid-state reaction of PbO (Sigma-Aldrich, ≥99.9%), $SrCO_3$ (Aldrich, ≥99.9%), and Fe_2O_3 (Sigma-Aldrich, ≥99.98%). The starting compounds were weighed according to the required stoichiometry, thoroughly ground, and pelletized. The heat treatment was conducted in several steps. After each step, the samples were reground and pressed into pellets again. The first two annealing steps were 750 °C, 15 h and 850 °C, 25 h for all of the samples. The temperature of the two subsequent steps was varied depending on the composition: 900 °C, 25 h (up to 22.5 atom % Sr), 950 °C, 25 h (from 25 to 60 atom % Sr), and 1000 °C, 25 h (from 60 to 100 atom % Sr). Following the same synthesis procedure, the $Pb_{0.792}Sr_{0.168}Fe_{1.040}O_{2.529}$ (17.5 atom % Sr) compound was synthetized in the amount of ~10 g for neutron powder diffraction (NPD) analysis.

Powder X-ray diffraction (XRD) was used to monitor evolution of the crystal structure upon increasing strontium content as well as the completeness of the reaction and the phase purity of the products. The XRD patterns were collected on a Huber G670 Guinier diffractometer [Cu Kα_1 radiation; curved Ge(111) monochromator; image plate]. The chemical composition of the samples was confirmed by energy-dispersive X-ray (EDX) analysis conducted on a JEOL 5510 scanning electron microscope equipped with an INCAx-sight 6587 system (Oxford Instruments). The EDX spectra from at least 30 crystallites were collected for each sample. The EDX results of the single-phase samples are listed in Table S1 in the Supporting Information.

NPD data were collected on the high-resolution powder diffractometer HRPT at the Laboratory for Neutron Scattering of Paul Scherrer Institute (LNS PSI, Villigen, Switzerland).[24] A powdered sample was placed in a vanadium container of 8 mm diameter. The NPD patterns have been collected at the wavelength 1.8857 Å in the 2θ range of 8–160° at temperatures of 300 and 900 K, using a custom-built tantalum radiation furnace.

Crystal structure analysis was performed with the *JANA2006* package.[25]

Transmission electron microscopy (TEM) was used in combination with the powder diffraction techniques for the crystal structure investigation. Electron diffraction (ED) patterns, high-angle annular dark-field scanning transmission electron microscopy (HAADF-STEM) images and EDX data were obtained using an FEI TecnaiG2 transmission electron microscope operated at 200 kV. Specimens for TEM investigation were prepared by grinding the samples in ethanol and depositing a few drops of the suspension on holey carbon grids.

The $Pb_{0.792}Sr_{0.168}Fe_{1.040}O_{2.529}$ sample enriched by 10% of ^{57}Fe was examined in a Mössbauer absorption study. A Mössbauer spectrum was collected using a conventional constant-acceleration spectrometer consisting of a nominal 1.85 GBq ^{57}Co radioactive source in a rhodium matrix mounted on an oscillating drive, secured on an optical rail with a sample stage and a gas proportional detector. The velocity scale was calibrated relative to a 25-μm-thick α-iron foil using the positions certified for (former) National Bureau of Standards standard reference material no. 1541; line widths of 0.28 mm/s for the outer lines of α-iron were obtained at room temperature. The dimensionless thickness of the sample was determined to be 4.6 based on the chemical composition and ^{57}Fe enrichment. Absorption spectra were fitted within the thin absorber approximation using the *MossA* fitting program.[26] The isomer shift values are given relative to the zero velocity of the α-iron calibration foil.

Magnetic susceptibility was measured on polycrystalline samples using Quantum Design MPMS SQUID in the temperature range 2–600 K in applied fields up to 7 T. Measurements above 400 K were performed in sealed quartz tubes filled with helium gas.

■ RESULTS

The composition of the anion-deficient perovskites modulated with periodic CS planes in the Pb–Sr–Fe–O system can be described with the general formula $(Pb_{1-z}Sr_z)_{1-x}Fe_{1+x}O_{3-y}$, where z is attributed to the Pb/Sr ratio, x stands for a small iron excess, and y is close to 0.5, maintaining the Sr^{2+}, Pb^{2+}, and Fe^{3+} oxidation states. The change of the CS plane orientation is mainly associated with a variable strontium content. Therefore, it is convenient to consider evolution of the system in relation to the z parameter. The following compositional ranges can be distinguished: (1) $0 < z < 0.05$, "$Pb_2Fe_2O_5$"-type defective structures;[27] (2) $0.05 \leq z \leq 0.2$, a series of incommensurately modulated perovskite-based compounds $(Pb_{1-z}Sr_z)_{1-x}Fe_{1+x}O_{3-y}$ with the $(h0l)_p$ orientation of the CS planes; the orientation changes from $(508)_p$ to $(90\underline{13})_p$ but stays close to $(203)_p$; (3) $0.2 < z < 0.3$, a two-phase region where compounds with the $(h0l)_p$ and $(101)_p$ CS planes coexist; (4) $0.3 \leq z \leq 0.45$, solid solution $(Pb_{1-z}Sr_z)_2Fe_2O_5$ with $(101)_p$ CS planes; the structures of these compounds are similar to that of the previously reported $Pb_{1.333}Sr_{0.667}Fe_2O_5$.[28]

In all of these ranges, the Fe cations retain the oxidation state 3+. Above $z = 0.45$, the samples demonstrate partial oxidation of Fe^{3+} to Fe^{4+}. Upon a further increase in the strontium content, the structure gradually transforms toward $SrFeO_3$. A detailed investigation of these Sr-rich compositions lies beyond the scope of this paper. Nevertheless, it is noteworthy that the perovskite-based structure modulated with the CS planes can be obtained if the Mn^{3+} cations are added into the system.[29]

$0.05 \leq z \leq 0.2$ Range: $(Pb_{1-z}Sr_z)_{1-x}Fe_{1+x}O_{3-y}$. According to the TEM data, the crystal structures of compounds in this compositional range are similar to that of $(Pb,Bi)_{1-x}Fe_{1+x}O_{3-y}$.[18] This is based on ordered arrays of equally spaced $(h0l)_p$ CS planes slicing the perovskite structure into quasi-2D blocks. The $[0\bar{1}0]$ ED pattern of $Pb_{0.792}Sr_{0.168}Fe_{1.040}O_{2.529}$, a representative member of the $(Pb_{1-z}Sr_z)_{1-x}Fe_{1+x}O_{3-y}$ series, is shown in Figure 1. This type of pattern is characteristic for the structures modulated with periodic planar interfaces. It is composed of parallel Bragg reflection arrays, centered at the positions of the basic perovskite reflections and oriented perpendicular to the CS planes. The ED pattern can be completely indexed using the superspace approach with the diffraction vectors $\mathbf{H} = h\mathbf{a}^* + k\mathbf{b}^* + l\mathbf{c}^* + m\mathbf{q}$, where $\mathbf{a}^*$, $\mathbf{b}^*$, and $\mathbf{c}^*$ are reciprocal vectors of the perovskite sublattice and $\mathbf{q} = \alpha\mathbf{a}^* + \gamma\mathbf{c}^*$ is a modulation vector.[30] The length of the $\mathbf{q}$ vector is inversely proportional to the doubled interplanar spacing between the CS planes in real space. The ED pattern indexation reveals a systematic reflection condition $h + k + l + m = 2n$ due to the superspace centering translation $[^1/_2, {}^1/_2, {}^1/_2, {}^1/_2]$, which suggests the (3 + 1)D space group $X2/m(\alpha 0\gamma)$ (where X stands for the centering vector) or its acentric subgroups. This group is a nonstandard setting of the $B2/m(\alpha\beta 0)$ superspace group.[31]

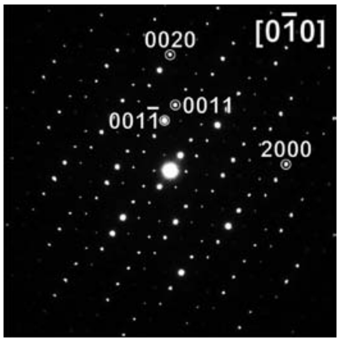

Figure 1. $[0\bar{1}0]$ ED pattern of $Pb_{0.792}Sr_{0.168}Fe_{1.040}O_{2.529}$.

The XRD patterns of $(Pb_{1-z}Sr_z)_{1-x}Fe_{1+x}O_{3-y}$ can be consistently indexed using ED data (Figure S1 in the Supporting Information). Evolution of the unit cell parameters and components of the modulation vector in the $(Pb_{1-z}Sr_z)_{1-x}Fe_{1+x}O_{3-y}$ series ($0.05 \leq z \leq 0.2$; Table 1) reveals systematic structural changes upon increasing strontium content. The most pronounced changes are associated with the orientation of the CS planes. The α component of the modulation vector gradually increases, while the γ component remains almost unchanged. The $(h0l)_p$ indexes describing the orientation of the CS planes with respect to the axes of the perovskite subcell are related to the components of the modulation vector as $h/l = \alpha/\gamma$. The h/l ratio varies from 0.6212 [$\sim(508)_p$ orientation] for $z = 0.05$ to 0.6876 [$\sim(90\underline{13})_p$ orientation] for $z = 0.2$. Thus, although the orientation of the CS planes systematically changes, it stays close to the $(203)_p$ plane ($h/l = 0.667$). The compositions listed in Table 1 are derived from the structural model describing the occupational modulation associated with the CS planes (see further in the text). These compositions are in a good agreement with the nominal compositions used for synthesis and have been confirmed by the EDX analysis (see Table S1 in the Supporting Information).

The $[0\bar{1}0]$ high-resolution HAADF-STEM image of $Pb_{0.792}Sr_{0.168}Fe_{1.040}O_{2.529}$ is shown in Figure 2. In this image, the intensity of the dots is proportional to the average atomic number of the projected columns and scales as Z^n, where $1.6 < n < 1.9$.[32] Pb-containing atomic columns appear as bright dots ($Z_{Pb} = 82$) and form square-pattern regions, which are attributed to the perovskite blocks. Weaker dots between the bright dots are the Fe–O columns ($Z_{Fe} = 26$; $Z_O = 8$). The pure oxygen columns are not visible. Sr ($Z_{Sr} = 38$) occupies part of the Pb positions in the perovskite blocks. The periodic CS planes are discernible by shorter projected distances between the (Pb, Sr)- and iron-containing columns (marked with arrowheads in Figure 2a). A similar atomic arrangement has been observed for the $(Pb,Bi)_{1-x}Fe_{1+x}O_{3-y}$ family.[18] Owing

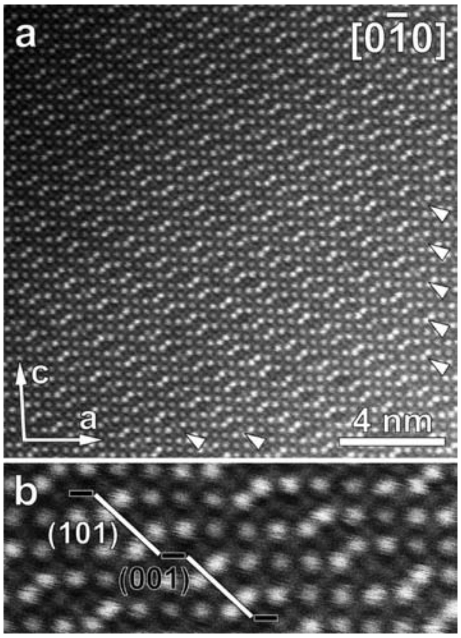

Figure 2. (a) High-resolution HAADF-STEM image of $Pb_{0.792}Sr_{0.168}Fe_{1.040}O_{2.529}$. The CS planes are indicated with arrowheads. (b) Enlarged fragment of the image showing segments of the 1/2[110](101)$_p$ and 1/2[110](001)$_p$ CS planes.

to this similarity, one can assume that the (3 + 1)D structure model constructed for $(Pb,Bi)_{1-x}Fe_{1+x}O_{3-y}$ can also be applied for $(Pb_{1-z}Sr_z)_{1-x}Fe_{1+x}O_{3-y}$. This model comprises a set of occupational domains defined for the A, B, and three O positions of the basic perovskite structure in the form of crenel functions.[33] It was built based on the concept that the $(h0l)_p$ CS planes can be represented as an ordered sequence of two parent fragments 1/2[110](001)$_p$ and 1/2[110](101)$_p$ (where 1/2[110] denotes the shear vector along the plane; see Figure 3 in ref 16; Figure 2b). The parameters of the crenel functions are expressed through the components of the modulation vector α and γ, which unequivocally define the orientation of the $(h0l)_p$ planes and the thickness of the perovskite blocks.

This structure model implies that the A-site cations are randomly distributed over all of the A positions in the structure. It is indeed a good approximation for the Pb^{2+} and Bi^{3+} cations in the $(Pb,Bi)_{1-x}Fe_{1+x}O_{3-y}$ family because they exhibit similar crystal chemistry and scattering power for both X-ray and neutron radiation. However, in the $(Pb_{1-z}Sr_z)_{1-x}Fe_{1+x}O_{3-y}$ structures, the difference in the scattering power and coordination preferences of the Pb^{2+} and Sr^{2+} cations is more pronounced. Taking into account that the A-site coordination environment at the CS planes is very asymmetric, only the lone-electron-pair cations Pb^{2+} can be accommodated in these positions. The A positions inside the perovskite blocks can be jointly occupied by the Sr^{2+} and Pb^{2+} cations. Such a cation distribution is also confirmed by the HAADF-STEM images, where the dots attributed to the A-site cations appear brighter at the CS planes rather than inside the perovskite blocks (Figure 2). A similar arrangement of Pb^{2+} and alkali-earth cations was found in the perovskite structures modulated by the 1/2[110](101)$_p$ CS planes.[34,21] The (3 + 1)D structure model for $(Pb_{1-z}Sr_z)_{1-x}Fe_{1+x}O_{3-y}$ was correspondingly modified to account for the partially ordered Pb^{2+} and Sr^{2+} cation distribution. The single A position occupational domain was split into three parts. One domain corresponds to the mixed Pb/Sr position inside the perovskite blocks, and the other two, related by an inversion center, correspond to the Pb positions at the CS planes on both sides of the perovskite blocks. The parameters of the model are summarized in Table 3. The details of the model construction are provided in the Supporting Information.

According to the superspace model, the composition of the $(Pb_{1-z}Sr_z)_{1-x}Fe_{1+x}O_{3-y}$ compounds is expressed through the components of the modulation vector by the formula $Pb_{4\alpha}(Pb,Sr)_{1-3\alpha-\gamma}Fe_{1-\alpha+\gamma}O_{3-\alpha-3\gamma}$. It defines the amount of Pb at the CS planes and (Pb, Sr) inside the perovskite blocks, Fe in the B positions, and the oxygen content. However, the Pb/Sr ratio cannot be directly calculated from the structure model. Therefore, to retrieve the composition of the compounds listed in Table 1, the Pb/Sr ratio was taken as that used for synthesis of the single-phase samples. The obtained cation compositions are in good agreement with the EDX data. Apart from the cation composition, the structural model adequately describes the oxygen content. The composition provided by the model corresponds to the iron oxidation state 3+, which is confirmed by Mössbauer spectroscopy (see below). One can calculate that the superspace model yields the same iron oxidation state for all compounds of the series. It is fully consistent with the almost

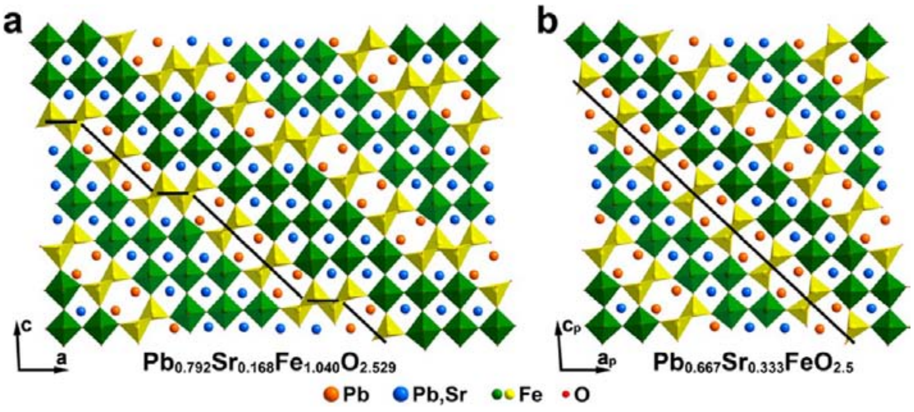

Figure 3. (a) Representative fragment of the $Pb_{0.792}Sr_{0.168}Fe_{1.040}O_{2.529}$ structure 12a × 1b × 8c. (b) Crystal structure of $Pb_{1.333}Sr_{0.667}Fe_2O_5$ plotted as a 8a_p × 1b_p × 8c_p supercell. The Fe atoms in octahedral and square-pyramidal coordination are shown in green and yellow, respectively; the A positions in the perovskite blocks are shown in blue and those in six-sided tunnels in orange. Horizontal and inclined lines represent fragments of the (001)$_p$ and (101)$_p$ CS planes, respectively.

invariant thickness of the perovskite blocks upon isovalent substitution of Pb^{2+} by Sr^{2+} (Table 1). A different situation was observed for $(Pb,Bi)_{1-x}Fe_{1+x}O_{3-y}$, where the anion deficiency depends on the Bi^{3+}/Pb^{2+} ratio and the thickness of the perovskite blocks increases upon increasing oxygen content.

The occupational superspace model reproduces the sequence of atomic layers inside the perovskite blocks and at the CS planes. However, it does not describe deformation of the perovskite framework induced by the periodically placed CS planes. To take this into account, modulation of the atomic displacements must be considered. This was done for the $Pb_{0.792}Sr_{0.168}Fe_{1.040}O_{2.529}$ compound during the Rietveld refinement of the structure using the NPD data. The material is antiferromagnetically ordered at room temperature, and the corresponding magnetic reflections appear on the NPD patterns. The magnetic structure solution of this incommensurately modulated phase is far from being trivial and will not be performed here. To avoid the magnetic contribution, the NPD data were collected at 900 K, well above the Néel temperature. The details on the Rietveld refinement are provided in the Supporting Information. The NPD profile after the Rietveld refinement is shown in Figure 4. Selected crystallographic data and the refinement parameters of $Pb_{0.792}Sr_{0.168}Fe_{1.040}O_{2.529}$ are given in Table 2. Atomic coordinates in the basic structure, parameters of the crenel functions, parameters of the displacive modulation functions, and the atomic displacement parameters (ADPs) are listed in Table 3. The distribution of the interatomic distances between the Fe, Pb/Sr, and Pb positions and the surrounding O atoms are plotted versus the internal coordinate t ($t = x_4 - \mathbf{q}\cdot\mathbf{r}$) in Figure 5.

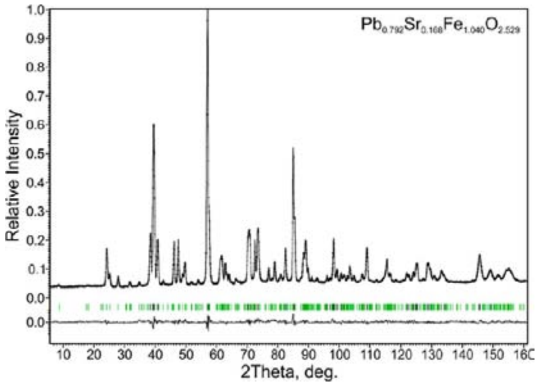

Figure 4. Experimental, calculated, and difference NPD patterns of $Pb_{0.792}Sr_{0.168}Fe_{1.040}O_{2.529}$ after Rietveld refinement. Black and green vertical bars indicate the positions of the main and satellite reflections, respectively.

Table 2. Selected Crystallographic Data and the Refinement Parameters of $Pb_{0.792}Sr_{0.168}Fe_{1.040}O_{2.529}$

formula	$Pb_{0.792}Sr_{0.168}Fe_{1.040}O_{2.529}$
space group	$X2/m(\alpha 0\gamma)$, $X = (^1/_2, ^1/_2, ^1/_2, ^1/_2)$
a, Å	3.9512(1)
b, Å	3.9483(1)
c, Å	3.9165(1)
β, deg	93.268(2)
$\mathbf{q}$	$0.0879(1)\mathbf{a}^* + 0.1276(1)\mathbf{c}^*$
calculated density, g/cm^3	7.55(2)
T, K	900
radiation	neutron, $\lambda = 1.494$ Å
2θ range; step, deg	$6 \le 2\theta \le 161$; 0.05
R_F (all reflections)	0.023
R_F (main reflections)	0.013
R_F (satellites of order 1−4)	0.022, 0.040, 0.037, 0.033
R_P, R_{wP}	0.029, 0.037

A representative $12a \times 1b \times 8c$ fragment of the $Pb_{0.792}Sr_{0.168}Fe_{1.040}O_{2.529}$ structure is shown in Figure 3a. Both $(001)_p$ and $(101)_p$ segments of the CS planes can be distinguished by the chains of distorted FeO_5 square pyramids connected through the common basal edges. The corresponding Fe positions are indicated in yellow. The $(001)_p$ segments correspond to the groups of four pyramids, and the $(101)_p$ segments correspond to the groups of two pyramids. Pyramidal chains together with the FeO_6 octahedra of the perovskite blocks delimit six-sided tunnels running along the b axis, which are filled with Pb^{2+} cations.

The ^{57}Fe Mössbauer spectroscopy data corroborate the chemical composition and structure of $Pb_{0.792}Sr_{0.168}Fe_{1.040}O_{2.529}$. In the room-temperature spectrum, the main contribution comes from two magnetic sextets denoted as O and P, which cover approximately 90% of the total absorption area (Figure 6). The minority contribution is attributed to the third magnetic sextet (denoted as T, ~5.4% of the total absorption) and to two paramagnetic doublets (denoted as E_1 and E_2; ~4.6% of the total absorption). Because $Pb_{0.792}Sr_{0.168}Fe_{1.040}O_{2.529}$ is magnetically ordered at room temperature, we assume that the paramagnetic doublets are of extrinsic origin. The chemical shifts for all contributions are characteristic for Fe cations in the oxidation state 3+ (Table S3 in the Supporting Information).[35] The sextet O with the largest chemical shift of 0.39 mm/s is attributed to octahedrally coordinated Fe^{3+} cations in the perovskite blocks. The linewidth (full width at half-maximum, fwhm) of this sextet is slightly larger than that of the Fe^{3+} cations in octahedral positions in similar structures, such as $PbBaFe_2O_5$.[35] This broadening is likely associated with the variable polar distortion of FeO_6 octahedra in the $Pb_{0.792}Sr_{0.168}Fe_{1.040}O_{2.529}$ structure (see Table 5 and the Discussion section). The sextet P with the smaller chemical shift of 0.32 mm/s can be attributed to the FeO_5-distorted tetragonal pyramids at the CS planes. The large broadening of this sextet (fwhm = 0.86 mm/s) likely arises from the presence of the groups of two and four edge-sharing FeO_5 pyramids, resulting in very distinct Fe−Fe contacts. In the double pyramidal chains, each Fe cation has two Fe nearest neighbors, whereas in the quadruple pyramidal chains, 50% of the Fe cations have four Fe nearest neighbors. The smaller chemical shift (0.305 mm/s) of the sextet T suggests that these Fe atoms have lower oxygen coordination, inferred to be tetrahedral. Although the refined structure does not contain tetrahedrally coordinated Fe positions, one can assume that a small fraction of FeO_4 tetrahedra can be formed in the perovskite blocks because of the presence of point oxygen vacancies. With this assumption, the atomic ratio of the Fe cations in the perovskite blocks and at the CS planes is 49:51 (as estimated from the relative areas of the contributing sextets), which is in agreement with the 51:49 ratio determined from the (3 + 1)D structure model (see the Supporting Information).

$0.3 \le z \le 0.45$ Range: Solid Solution $(Pb_{1-z}Sr_z)_2Fe_2O_5$. A member of this solid solution with $z = 0.333$, $Pb_{1.333}Sr_{0.667}Fe_2O_5$, was investigated earlier.[28] It has a perovskite-based structure modulated with the $(101)_p$ CS planes.

Table 3. Occupational Model of the $(Pb_{1-z}Sr_z)_{1-x}Fe_{1+x}O_{3-y}$ $(0.05 \le z \le 0.2)$ Series of Structures, Numerical Values of Δ, Parameters of the Displacive Modulation, and ADPs for $Pb_{0.792}Sr_{0.168}Fe_{1.040}O_{2.529}$

atom	x, y, z	$x_{4,0}$	Δ	displacive modulation parameters[b]		ADP,[c] Å^2		
Fe	0, 0, 0	0	$(1-\alpha+\gamma)/2$	$S_{x,1} = 0.0031$,	$S_{z,1} = 0.0638$,	$U_{iso} = 0.0208(3)$		
			0.5198	$S_{x,3} = -0.041(2)$	$S_{z,3} = 0.042(2)$			
PbSr[a]	0, 0, 0	$^1/_2$	$(1-3\alpha-\gamma)/2$	$A^s_{x,1} = 0.0720$,	$A^s_{z,1} = 0.0131$,	$U_{iso} = 0.049(1)$		
			0.3043	$A^s_{x,2} = -0.047(1)$	$A^s_{z,2} = 0.043(1)$			
Pb	0, 0, 0	$(1+\alpha+\gamma)/4$	α	$A^s_{x,1} = 0.0720$,	$A^s_{z,1} = 0.0131$,	$U_{iso} = 0.031(1)$		
			0.0879	$A^s_{x,2} = -0.047(1)$	$A^s_{z,2} = 0.043(1)$			
O1	0, $^1/_2$, 0	0	$(1-\alpha+\gamma)/2$	$S_{x,1} = 0.0456$,	$S_{z,1} = 0.2284$,	$U_{eq} = 0.040(1)$		
			0.5198	$S_{x,3} = -0.051(4)$	$S_{z,3} = 0.049(3)$	$U_{11} = 0.061(2)$	$U_{22} = 0.015(1)$	$U_{33} = 0.045(3)$
						$U_{12} = 0$	$U_{13} = 0$	$U_{23} = 0$
O2	$^1/_2$, 0, 0	0	$(1+\alpha-3\gamma)/2$	$S_{x,1} = 0.0459$,	$S_{z,1} = 0.1511$,	$U_{eq} = 0.034(1)$		
			0.3525	$S_{x,3} = 0$	$S_{z,3} = 0.060(6)$	$U_{11} = 0.019(2)$	$U_{22} = 0.044(2)$	$U_{33} = 0.039(3)$
						$U_{12} = 0$	$U_{13} = 0$	$U_{23} = 0$
O3	0, 0, $^1/_2$	0	$(1-\alpha-\gamma)/2$	$S_{x,1} = 0.0438$,	$S_{z,1} = 0.1100$,	$U_{eq} = 0.041(2)$		
			0.3922	$S_{x,3} = -0.042(8)$	$S_{z,3} = 0.027(7)$	$U_{11} = 0.047(3)$	$U_{22} = 0.052(2)$	$U_{33} = 0.025(2)$
						$U_{12} = 0$	$U_{13} = 0.004(2)$	$U_{23} = 0$

[a] The occupancy factor 0.724Pb + 0.276Sr. It is given by the $\xi = 1 - z[(1+\alpha-\gamma)/(1-3\alpha-\gamma)]$ parameter (see the Supporting Information). [b] The atomic displacement modulation of the PbSr and Pb atoms is restricted to that of the imaginary atom AUX. It is modulated with the harmonic functions: $\mathbf{r}^{AUX} = \mathbf{r}_0^{AUX} + \sum_n\{\mathbf{A}_n^s \sin(2\pi n x_4) + \mathbf{A}_n^c \cos(2\pi n x_4)\}$. The modulation of other atoms (Fe1, O1, O2, and O3) is given by $\mathbf{r}^\nu = \mathbf{r}_0^\nu + \sum_n\{\mathbf{S}_{2n-1}^\nu P_{2n-1}[2(x_4 - x_{4,0})/\Delta] + \mathbf{S}_{2n}^\nu P_{2n}[2(x_4 - x_{4,0})/\Delta]\}$. In these equations, $\mathbf{r}^\nu$ is the position of atom ν, $\mathbf{r}_0^\nu$ is the basic position of atom ν, n is the order of the modulation wave, and $P_n(x) = [1/(2^n n!)](d^n/dx^n)[(x^2-1)^n]$ are the Legendre polynomials. Polynomials of two orders are required to describe one order of the modulation wave; i.e., P_1 and P_2 form the first modulation wave, P_3 and P_4 the second wave, etc. The A_n and $\mathbf{S}_n^\nu$ parameters are the coefficients in expansion. The first-order coefficients $\mathbf{S}_1^\nu$ are the maximum linear displacements of atom ν. The $X2/m(\alpha 0\gamma)$ $[X = (^1/_2, {}^1/_2, {}^1/_2, {}^1/_2)]$ symmetry rules out even modulation of the atoms, so $\mathbf{A}_n^c = 0$, $\mathbf{S}_{even} = 0$, $\mathbf{r}^{AUX} = \mathbf{r}_0^{AUX} + \sum_n\{\mathbf{A}_n^s \sin(2\pi n x_4)\}$, and $\mathbf{r}^\nu = \mathbf{r}_0^\nu + \sum_n\{\mathbf{S}_{2n-1}^\nu P_{2n-1}[2(x_4 - x_{4,0})/\Delta]\}$. [c] The anisotropic temperature factor has the form $t^\nu = \exp(-2\pi^2\sum_i\sum_j U_{ij}^\nu a_i a_j h_i h_j)$; $U_{eq}^\nu = 1/3\sum_i\sum_j U_{ij}^\nu a_i a_j \mathbf{a}_i \mathbf{a}_j$.

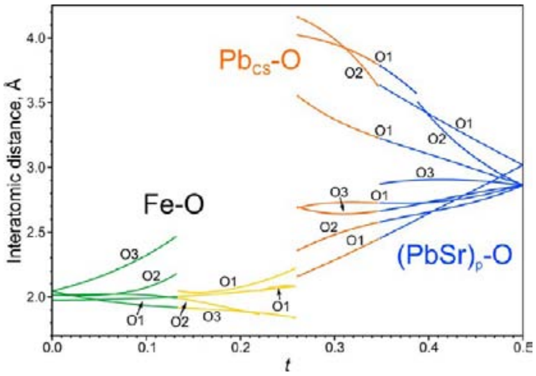

Figure 5. t plot of the Fe−O, Pb−O, and PbSr−O interatomic distances in the $Pb_{0.792}Sr_{0.168}Fe_{1.040}O_{2.529}$ structure. The symmetry-related atomic domains are marked identically. The colors correspond to those chosen for the structure representation in Figure 3.

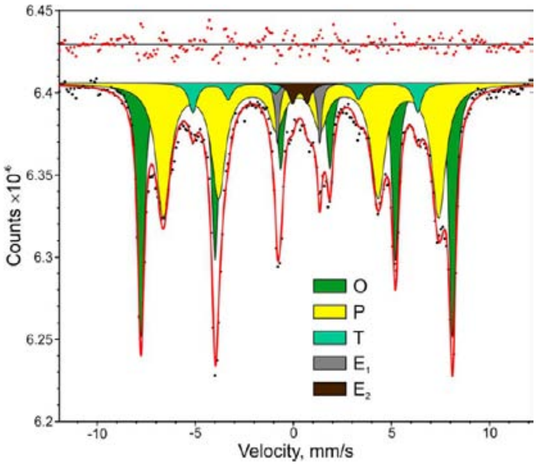

Figure 6. Room-temperature ^{57}Fe Mössbauer spectrum of $Pb_{0.792}Sr_{0.168}Fe_{1.040}O_{2.529}$. Different contributions are color-coded (see the text and Table S3 in the Supporting Information).

The crystal structure is described on the orthorhombic lattice with the *Pnma* space group and the unit cell parameters related to those of the basic perovskite structure as $a \approx \sqrt{2}a_p$, $b \approx a_p$, and $c \approx 4\sqrt{2}a_p$. We have established that the lead/strontium content can be varied without altering the structure in the $0.3 \le z \le 0.45$ range. The unit cell parameters for different z values are listed in Table 4. Typical XRD and ED patterns of $(Pb_{1-z}Sr_z)_2Fe_2O_5$ are represented in Figures S5 and S6 in the Supporting Information, respectively. The composition of the compounds was confirmed by EDX analysis (Table S1 in the Supporting Information).

The crystal structure of $(Pb_{1-z}Sr_z)_2Fe_2O_5$ is illustrated in Figure 3b. It is shown as an $8a_p \times 1b_p \times 8c_p$ supercell, so it can be easily compared to the $(Pb_{1-z}Sr_z)_{1-x}Fe_{1+x}O_{3-y}$ structure in the $0.05 \le z \le 0.2$ range. These structures share the same building principles. They are based on the perovskite framework fragmented by periodic CS planes. However, the orientation of the planes is different. In $(Pb_{1-z}Sr_z)_2Fe_2O_5$ and $(Pb_{1-z}Sr_z)_{1-x}Fe_{1+x}O_{3-y}$, the CS planes lie upon the $(101)_p$ and $(h0l)_p$ (h/l = 0.621−0.688) lattice planes, respectively. In the HAADF-STEM images, the $(101)_p$ CS planes $(Pb_{1-z}Sr_z)_2Fe_2O_5$ appear as rows of double lead columns running parallel to the a axis of the orthorhombic lattice or the $[10\bar{1}]_p$ direction of the perovskite sublattice (Figure 7).

Intermediate Range 0.2 < *z* < 0.3. In this compositional range, the phases with the $(101)_p$ and $(h0l)_p$ CS planes coexist (see Figure S7 in the Supporting Information). Besides the macroscopic phase separation, the structures form coherent intergrowths on a nanoscale level. A representative $[0\bar{1}0]$ HAADF-STEM image of a crystal comprising domains of both

Table 4. Evolution of the Cell Parameters of $(Pb_{1-z}Sr_z)_2Fe_2O_5$ $(0.3 \leq z \leq 0.45)$

		cell parameters				perovskite sublattice parameters			
composition	z	a, Å	b, Å	c, Å	V, Å^3	$a_p = c_p$, Å	b_p, Å	β, deg	V_p, Å^3
$Pb_{1.4}Sr_{0.6}Fe_2O_5$	0.3	5.6886(2)	3.9247(1)	21.1179(8)	471.47(5)	3.880	3.925	94.272	58.935
$Pb_{1.33}Sr_{0.67}Fe_2O_5$	0.335	5.6880(2)	3.9240(1)	21.1133(6)	471.24(4)	3.880	3.924	94.279	58.905
$Pb_{1.3}Sr_{0.7}Fe_2O_5$	0.35	5.6841(1)	3.9229(1)	21.1036(4)	470.57(6)	3.878	3.923	94.266	58.821
$Pb_{1.2}Sr_{0.8}Fe_2O_5$	0.4	5.6825(1)	3.9220(1)	21.0900(4)	470.02(5)	3.876	3.922	94.287	58.753
$Pb_{1.1}Sr_{0.9}Fe_2O_5$	0.45	5.6796(1)	3.9212(1)	21.0827(4)	469.52(6)	3.874	3.921	94.277	58.691

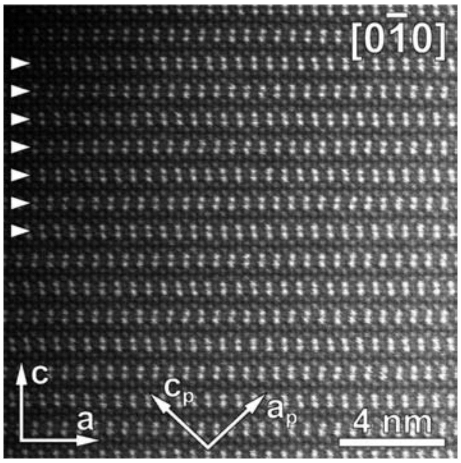

Figure 7. High-resolution HAADF-STEM image of $Pb_{1.2}Sr_{0.8}Fe_2O_5$. The CS planes are indicated with arrowheads.

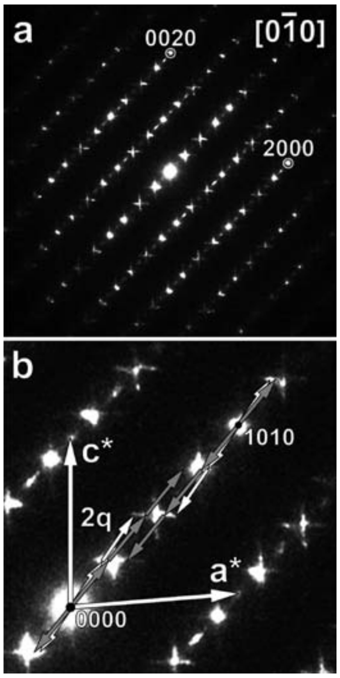

Figure 9. (a) ED pattern of the intergrowth crystal with the varying orientations of the CS planes. (b) Enlarged fragment of the pattern showing that the diffuse intensity streaks appear because of the variable modulation vector (white and gray arrows).

structures is shown in Figure 8. The $(101)_p$ and $(h0l)_p$ CS planes are marked with white and dark lines, respectively. The boundaries between the domains lie on the $(100)_p$ and $(001)_p$ planes. The coherent intergrowths of these structures are formed owing to a similar thickness of the perovskite blocks and very close parameters of the perovskite subcell (compare data in Tables 1 and 4).

The corresponding $[0\bar{1}0]$ ED pattern of the intergrowth crystal is shown in Figure 9a. The pattern combines features specific to both structures. The intensity maxima of the Bragg reflections are positioned in accordance with the reciprocal lattice of the $(Pb_{1-z}Sr_z)_2Fe_2O_5$ structure modulated with $(101)_p$ CS planes. The reflections are arranged in rows parallel to the $[101]_p$ reciprocal direction. Many of these reflections exhibit cross-shaped diffuse intensity, with the constituting streaks oriented along the **a*** and **c*** directions. The streaks along **a*** can be interpreted as a set of closely positioned satellite

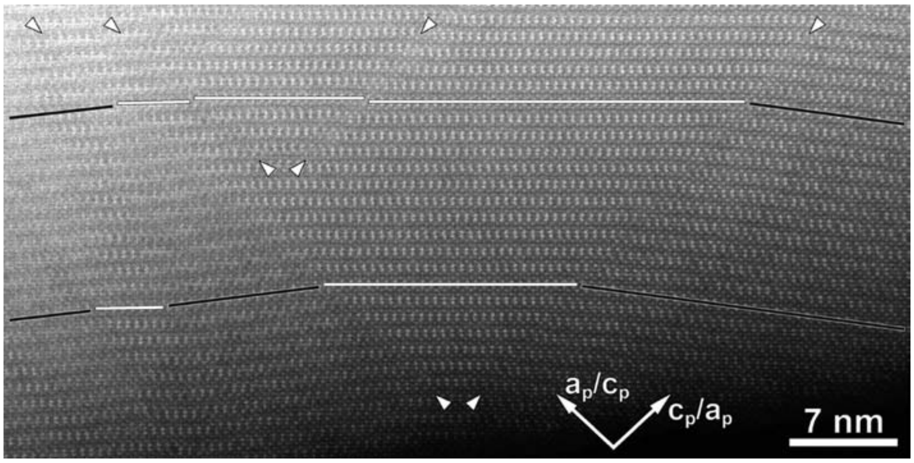

Figure 8. HAADF-STEM image of $(Pb_{1-z}Sr_z)_{1-x}Fe_{1+x}O_{3-y}$ ($z = 0.225$) showing the intergrowth of the domains with different orientations of the CS planes. The boundaries between the domains with $(101)_p$ planes and the domains with $(h0l)_p$ planes are indicated with arrowheads. The fragments of $(101)_p$ and $(h0l)_p$ planes are marked with white and dark lines, respectively.

reflections originating from the domains, with the CS plane orientation deviating from $(101)_p$. A schematic representation of the corresponding **q**-vector variation is illustrated in Figure 9b. Similar to evolution of the single-phase $(Pb_{1-z}Sr_z)_{1-x}Fe_{1+x}O_{3-y}$ compounds, the **q** vector changes the orientation mainly because of the α component, whereas the γ component remains nearly unchanged. The diffuse intensity streaks along the **c*** axis are of the same origin. However, they arise from the domains with the CS plane orientation flipped with respect to the $(10\overline{1})_p$ plane (compare the domains on the right- and left-hand sides of the HAADF-STEM image in Figure 8).

Magnetic Properties. We studied the magnetic behavior of two samples, $Pb_{0.792}Sr_{0.168}Fe_{1.040}O_{2.529}$ (z = 0.175) and $Pb_{1.2}Sr_{0.8}Fe_2O_5$ (z = 0.4), which are representative of the structures modulated with the $(h0l)_p$ ($0.05 \leq z \leq 0.2$) and $(101)_p$ ($0.3 \leq z \leq 0.45$) CS planes, respectively (Figure 10). At first glance, these two samples show drastically different magnetic behavior. The susceptibility of $Pb_{0.792}Sr_{0.168}Fe_{1.040}O_{2.529}$ is weakly field-dependent and increases with the temperature. The $Pb_{0.6}Sr_{0.4}FeO_{2.5}$ sample shows a much higher susceptibility and therefore is strongly field-dependent and decreases upon heating. This difference is due to a minor ferromagnetic component present in the $Pb_{0.6}Sr_{0.4}FeO_{2.5}$ sample. Unfortunately, reliable measurements above 600 K are not possible because both samples decompose in the inert atmosphere (sealed quartz tube filled with helium gas). Nevertheless, the data tentatively collected above 600 K show clearly that the ferromagnetic signal of the $Pb_{0.6}Sr_{0.4}FeO_{2.5}$ sample disappears around 740 K, which is close to the Curie point of $PbFe_{12}O_{19}$.[36] Therefore, we ascribe this ferromagnetic signal to a minor impurity of lead hexaferrite or similar phases. A remnant magnetization of just 0.1 μ_B/fu (see the Supporting Information) corresponds to less than 0.5 wt % of the impurity phase that cannot be observed by standard characterization techniques.

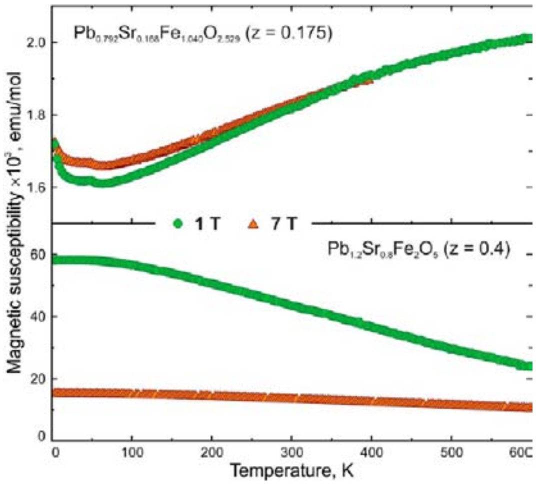

Figure 10. Magnetic susceptibility of $Pb_{0.792}Sr_{0.168}Fe_{1.040}O_{2.529}$ (z = 0.175, top panel) and $Pb_{1.2}Sr_{0.8}Fe_2O_5$ (z = 0.4, bottom panel) measured in applied fields of 1 and 7 T.

Below 600 K, the susceptibility of $Pb_{0.792}Sr_{0.168}Fe_{1.040}O_{2.529}$ shows only a weak temperature dependence, as expected for a collinear antiferromagnet below its Néel temperature T_N. We expect that the Néel temperatures of both $Pb_{0.792}Sr_{0.168}Fe_{1.040}O_{2.529}$ and $Pb_{0.6}Sr_{0.4}FeO_{2.5}$ are above 600 K, similar to $Pb_{1.08}Ba_{0.92}Fe_2O_5$ (T_N = 625[34]) and $Pb_{0.64}Bi_{0.32}Fe_{1.04}O_{2.675}$ (T_N = 608 K[18]). A small but reproducible kink at 48 K in the susceptibility of $Pb_{0.792}Sr_{0.168}Fe_{1.040}O_{2.529}$ might indicate another magnetic transition (e.g., spin reorientation). Details of this transition require further investigation.

■ DISCUSSION

The perovskite-based structures modulated by periodic CS planes exist in a wide range of strontium concentrations. At low strontium content, the orientation of the CS planes in the $(Pb_{1-z}Sr_z)_{1-x}Fe_{1+x}O_{3-y}$ series ($0.05 \leq z \leq 0.2$) systematically changes but stays close to $(203)_p$. This is accompanied by a slight variation in the thickness of the perovskite blocks (see Table 1), which is required to maintain the 3+ oxidation state of the Fe cations. A further increase in the strontium content stabilizes the $(101)_p$ CS planes. These planes are preserved in the $0.3 \leq z \leq 0.45$ range and result in the structure of the $(Pb_{1-z}Sr_z)_2Fe_2O_5$ solid solution. Such behavior of the CS planes in the Pb−Sr−Fe−O system can be understood by analyzing distortion of the perovskite blocks in each compositional range.

An enlarged fragment of the $Pb_{0.792}Sr_{0.168}Fe_{1.040}O_{2.529}$ crystal structure is shown in Figure 11. At the center of the perovskite block, the FeO_6 octahedra are weakly distorted and feature six almost equal Fe−O distances (Table 5). The octahedra on the left- and right-hand sides from the central FeO_6 octahedron acquire noticeable distortion by shortening one of the Fe−O bonds along the c axis. The coordination number of these Fe atoms can be represented as 1 + 4 + 1, with one short, one long, and four intermediate Fe−O bonds (Table 5). The degree of distortion that the FeO_6 octahedra gain on going from the center toward the periphery of the perovskite blocks is best illustrated by evolution of an octahedral distortion parameter as a function of the t coordinate (Figure 12a). The parameter measures the distortion as a mean-square relative deviation of the Fe−O bond length from the average: $\Delta_{oct} = 1/6\sum_{i=1}^{6}[(l_i - \overline{l})/\overline{l}]^2$, where l_i is the Fe−O bond length and $\overline{l}$ is the average over all six Fe−O distances in the octahedron.[37] At the center of the perovskite block (t = 0), the parameter is small, $\Delta_{oct} = 0.2 \times 10^{-3}$, but it rapidly increases to $\Delta_{oct} = 7.8 \times 10^{-3}$ for the octahedra near the CS planes (t = 0.132). For reference, the degree of distortion can be compared with the off-center displacement of the Ti^{4+} cations in $PbTiO_3$, which also occurs

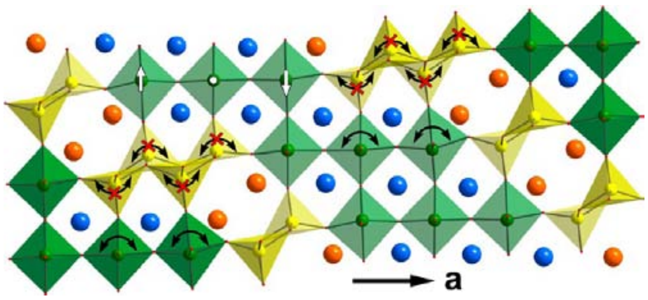

Figure 11. Enlarged fragment of the $Pb_{0.792}Sr_{0.168}Fe_{1.040}O_{2.529}$ structure. The white arrows indicate (exaggeratedly) the displacement of the Fe^{3+} cations from the basal planes of the octahedra, which results in one short, one long, and four intermediate Fe−O distances. The black arrows demonstrate that the rotation of the octahedra connected to the rigid chains of quadruple tetragonal pyramids is prevented, unless there is significant distortion of the Fe−O polyhedra.

Table 5. Fe–O Interatomic Distances in the FeO_6 Octahedra in the Perovskite Blocks of $Pb_{0.792}Sr_{0.168}Fe_{1.040}O_{2.529}$[a]

distance[b,c]	$t = 0$	$t = 0.132$	min	max	average
$Fe-O1^1$	1.9742	2.002(2)	1.9742	2.002(2)	1.98
$Fe-O1^2$	1.9742	2.002(2)	1.9742	2.002(2)	1.98
$Fe-O2^1$	2.013(9)	2.18(2)	2.01(1)	2.18(2)	2.05
$Fe-O2^2$	2.013(9)	1.99(3)	1.99(3)	2.023(5)	2.02
$Fe-O3^1$	2.045(14)	2.469(14)	2.045(14)	2.469(14)	2.22
$Fe-O3^2$	2.045(14)	1.918(18)	1.918(18)	2.045(14)	1.97

[a] The distances at the center of the blocks correspond to $t = 0$; near the CS planes – to $t = 0.132$. [b] The distances are measured in angstroms. [c] Superscripts 1 and 2 indicate the Fe–O distances to the symmetry equivalent O atoms, i.e. $O1^1(x,y,z)$ and $O1^2(x,y-1,z)$; $O2^1(x,y,z)$ and $O2^2(x-1,y,z)$; $O3^1(x,y,z)$ and $O3^2(x,y,z-1)$.

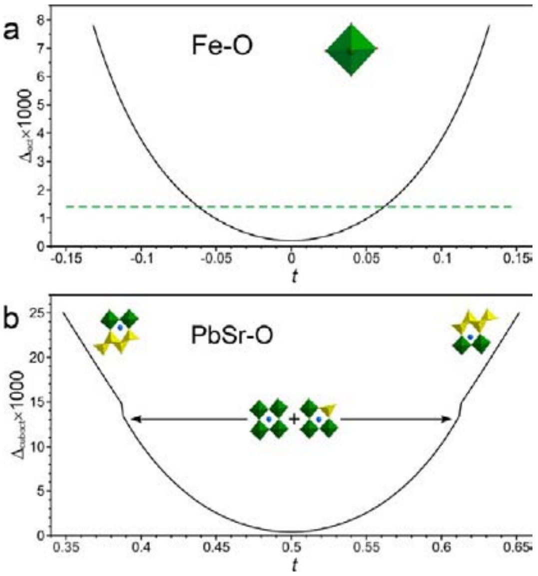

Figure 12. t plots of the octahedral (a) and cuboctahedral (b) distortion parameters of the perovskite blocks in the $Pb_{0.792}Sr_{0.168}Fe_{1.040}O_{2.529}$ structure. The dotted line indicates the value of Δ_{oct} of the $Pb_{1.333}Sr_{0.667}Fe_2O_5$ structure.

toward one of the O atoms. The corresponding $\Delta_{oct}(PbTiO_3)$, calculated from the structural data in ref 38, is 4.3×10^{-3}. However, in contrast to ferroelectric $PbTiO_3$, in $Pb_{0.792}Sr_{0.168}Fe_{1.040}O_{2.529}$ local dipoles on the opposite sides of the perovskite block are antiparallel and compensate each other, thus forming an antipolar structure.

The antipolar distortion is also supported by the displacement of the A cations within the perovskite block. They shift along the c axis toward the O1 and O2 atoms, which form the square bases of the FeO_6 octahedra and the FeO_5 tetragonal pyramids (Figure 3). This results in a highly asymmetric coordination environment for these A positions, with some short and some long PbSr–O distances (Figure 5). Apparently, this asymmetry is promoted by the hybridization of the Pb 6p states with the antibonding [Pb 6s–O 2p]* states, which is generally considered to be the effect of a stereochemically active lone electron pair.[39] Similar to the octahedral distortion parameter, deformation of the A cation coordination environment can be quantified with a cuboctahedral distortion parameter: $\Delta_{cuboct} = 1/12\sum_{i=1}^{12}[(l_i - \bar{l})/\bar{l}]^2$; here l_i and $\bar{l}$ are the PbSr–O distances and average, respectively. The t plot of the Δ_{cuboct} parameter is shown in Figure 12b. It demonstrates a trend similar to that of Δ_{oct}. At the center of the perovskite block, the distortion of the A cation cuboctahedral coordination is negligible ($\Delta_{cuboct} = 0.4 \times 10^{-3}$), but it increases drastically for the positions next to the CS planes ($\Delta_{cuboct} = 25.1 \times 10^{-3}$).

In the $(Pb_{1-z}Sr_z)_2Fe_2O_5$ structure modulated by $(101)_p$ CS planes ($0.3 \leq z \leq 0.45$), the pattern of atomic displacements is somewhat different. The PbSr and Fe coordination environment becomes distorted along the c axis of the orthorhombic lattice, which is equivalent to the $[101]_p$ direction of the perovskite sublattice. In the $Pb_{1.333}Sr_{0.667}Fe_2O_5$ structure, the octahedra demonstrate four Fe–O bonds of similar length (1.97 Å × 2, 1.94 Å, and 1.96 Å) and two longer ones (2.12 and 2.11 Å).[28] The resulting octahedral distortion parameter $\Delta_{oct} = 1.4 \times 10^{-3}$ is substantially lower than that for the octahedral positions near the CS planes in $Pb_{0.792}Sr_{0.168}Fe_{1.040}O_{2.529}$. The octahedral distortions in these structures are compared in Figure 12a, where the value of $\Delta_{oct}(Pb_{1.333}Sr_{0.667}Fe_2O_5)$ is indicated with a dotted line.

A visual inspection of the $Pb_{1.333}Sr_{0.667}Fe_2O_5$ structure reveals that within the perovskite blocks the distortion of the A-site coordination environment is associated with the displacement of the A cations from the center of the cuboctahedra along the $[101]_p$ direction as well as with the cooperative tilt of the FeO_6 octahedra about the b axis. Apparently, the octahedral tilt is necessary to compensate for the mismatch of the A–O and Fe–O interatomic distances in the perovskite blocks. Although a distance mismatch exists in the entire compositional range $0.05 \leq z \leq 0.45$, there is no octahedral tilt in the $(Pb_{1-z}Sr_z)_{1-x}Fe_{1+x}O_{3-y}$ series ($0.05 \leq z \leq 0.2$). The bands of quadruple edge-sharing FeO_5 tetragonal pyramids are rigid fragments in the $(Pb_{1-z}Sr_z)_{1-x}Fe_{1+x}O_{3-y}$ structure; they suppress the octahedral rotation. As can be seen in Figure.11, the connection topology between these bands and the octahedra of the perovskite blocks does not allow the octahedral tilt about the b axis without introducing an unfavorable strain. In this structure, the bond distance mismatch is relieved through deformation of the Fe–O framework. In the structure of the $(Pb_{1-z}Sr_z)_2Fe_2O_5$ solid solution ($0.3 \leq z \leq 0.45$), only the chains of double edge-sharing FeO_5 pyramids are present at the CS planes. These chains can tilt left or right following the FeO_6 octahedra of the perovskite blocks and do not restrict the octahedral tilting (Figure 13).

In the $(Pb_{1-z}A_z)_2Fe_2O_5$ (A = Sr, Ba) structures, the octahedral tilt depends on the average ionic radius of the A cation. It can be suppressed by introducing larger A-site cations, such as Ba^{2+} [$r(Ba^{2+})_{XII}$ = 1.61 Å],[23] without altering the structure. In $Pb_{1.33}Sr_{0.67}Fe_2O_5$, the angle of the octahedral tilt is about 7° (the exact value cannot be measured unequivocally because of the octahedral distortion). In the $Pb_{1.33}Sr_{0.67-x}Ba_xFe_2O_5$ solid solution, this value gradually decreases to ~4° for $Pb_{1.33}Sr_{0.33}Ba_{0.33}Fe_2O_5$.[40] Increasing the

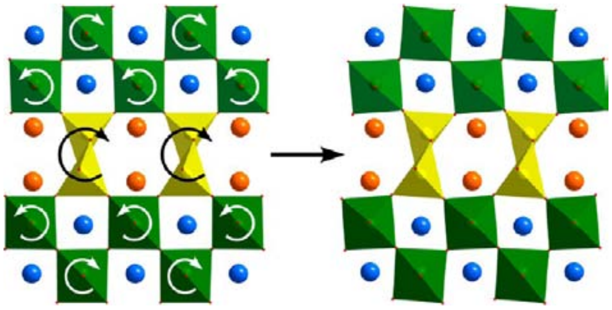

Figure 13. Contribution of the double edge-sharing pyramidal chains to the cooperative tilt of the octahedra about the *b* axis in the $(Pb_{1-z}Sr_z)_2Fe_2O_5$ structure.

size of the A-site cation suppresses the octahedral tilt even further, down to ∼1° in $Pb_{1.08}Ba_{0.92}Fe_2O_5$.[21] In this limiting case, the A position coordination environment in the perovskite blocks demonstrates almost no distortions ($\Delta_{\text{cuboct}} = 0.5 \times 10^{-3}$), whereas the octahedral distortion is similar to that in $Pb_{1.333}Sr_{0.667}Fe_2O_5$ with $\Delta_{\text{oct}}(Pb_{1.08}Ba_{0.92}Fe_2O_5) = 1.7 \times 10^{-3}$. Thus, the $(Pb_{1-z}A_z)_2Fe_2O_5$ (A = Sr, Ba) structures exist with both well-pronounced and suppressed octahedral tilt. In spite of a sufficient difference of the ionic radii of Pb^{2+} and Ba^{2+} [$r(Pb^{2+})_{XII}$ = 1.49 Å; $r(Ba^{2+})_{XII}$ = 1.61 Å],[23] the reported *z* homogeneity range of the $(Pb_{1-z}Ba_z)_2Fe_2O_5$ structures is very similar to that of $(Pb_{1-z}Sr_z)_2Fe_2O_5$, established in this work. Therefore, one can speculate that the ionic radii mismatch is not the main factor influencing the orientation of the CS planes. To clarify the role of this factor, a structure with even smaller A-site cations should be considered. However, to date, no perovskite CS structures are known with non-lone-electron-pair A cations smaller than Sr^{2+}.

Major factors that control the orientation of the CS planes are associated with the stereochemical activity of the Pb^{2+} cations. The structure with the $(101)_p$ CS planes creates an unfavorable bonding situation for the lone-pair cations located inside the perovskite blocks. For the Pb^{2+} cations in $(Pb_{1-z}Sr_z)_2Fe_2O_5$, the displacements in the neighboring unit cells of the perovskite block are always antiparallel, thus causing a competition of two lone-pair cations for the 2p orbitals of the same O atoms (Figure 14). Apparently, such a structure would be stabilized when the lone-pair cations in the perovskite blocks are largely replaced by alkali-earth cations. Changing the orientation of the CS planes by introducing the $(001)_p$ segments increases the number of A positions in the perovskite blocks along the *a* direction. As can be seen from the scheme in Figure 14, this significantly reduces the number of unfavorable A cation pairs, thus making the perovskite blocks more suitable for accommodation of the lone-pair cations. This trend is consistent with evolution of the CS plane orientation in the $0.05 \leq z \leq 0.2$ compositional range, where upon an increase in the Pb concentration, the fraction of the $(001)_p$ segments on the CS planes increases (the α/γ ratio decreases). Furthermore, it is in accordance with the $\sim(509)_p$ orientation of the CS planes in the $(Pb,Bi)_{1-x}Fe_{1+x}O_{3-y}$ family, where the A positions are occupied exclusively by the lone-electron-pair cations Pb^{2+} and Bi^{3+}. A complete elimination of the alkali-earth cations significantly reduces the fraction of the $(101)_p$ segments on the CS planes $(\alpha/\gamma)[(Pb,Bi)_{1-x}Fe_{1+x}O_{3-y}] < (\alpha/\gamma)$-$[(Pb_{1-z}Sr_z)_{1-x}Fe_{1+x}O_{3-y}]$). However, the $(101)_p$ segments cannot be eliminated completely from the anion-deficient perovskite structure because they are responsible for reducing the oxygen content. The displacement vector $1/2[110]_p$ of the CS plane has no component orthogonal to the $(001)_p$ segments, and this type of plane cannot change the oxygen content of the structure.[17]

Another factor governing the orientation of the CS planes is a fraction of the A positions located at the CS planes with respect to that in the perovskite blocks. In the Pb−Sr−Fe−O system, upon a decrease in the concentration of the lone-electron Pb^{2+} cations, the perovskite blocks become less flexible and cannot accommodate the structure distortions associated with the presence of the $(001)_p$ CS plane fragments. In this case, the structure with the $(101)_p$ CS planes is stabilized because it causes much lower distortion of the perovskite framework. Changing the orientation of the CS planes redistributes the Pb^{2+} cations in the structure. To illustrate this, the fraction of the A positions inside the hexagonal tunnels at the CS plane can be quantified with the parameter $\psi = 4\alpha/(1 + \alpha - \gamma) \times 100\%$ (see the Supporting Information for details). In other words, the ψ parameter stands for the fraction of A positions with a strongly asymmetric coordination and occupied exclusively by the Pb^{2+} cations. In the $(Pb_{1-z}Sr_z)_{1-x}Fe_{1+x}O_{3-y}$ series, ψ varies from 33.5% (z = 0.05) to 36.9% (z = 0.2), whereas in the structure of the $(Pb_{1-z}Sr_z)_2Fe_2O_5$ solid solution, ψ = 50%. Thus, in the structure with the $(101)_p$ CS planes, the Pb^{2+} cations are accumulated at the CS planes in the asymmetric coordination without introducing unfavorable distortions of perovskite

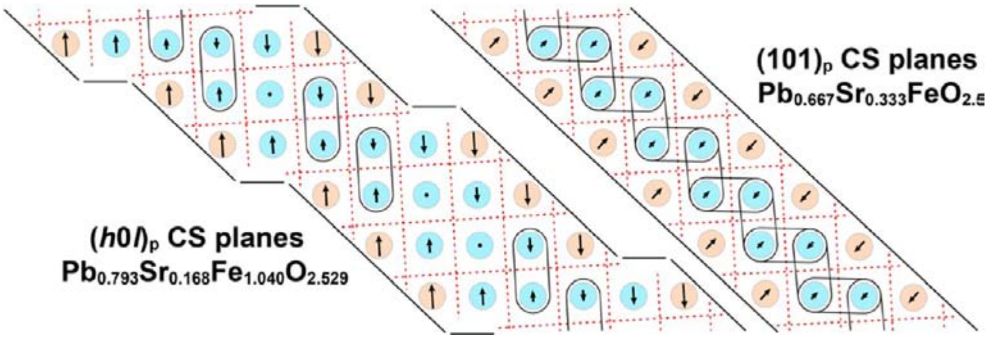

Figure 14. Schematic representation of the A cation and anion sublattice distortions in the perovskite blocks of the structures with the $(h0l)_p$ and $(101)_p$ CS planes. The displacement of the A-site cations is shown with exaggerated arrows. The $(101)_p$ and $(001)_p$ CS plane segments are indicated with horizontal and inclined black lines, respectively. The red dotted lines correspond to the planes formed by the O atoms. Pairs of adjacent A cations shifting toward the same O layer are enclosed in ovals.

blocks. It is noteworthy that the fraction of Fe^{3+} cations in the square-pyramidal coordination at the CS planes does not change significantly in the entire compositional range $0.05 \leq z \leq 0.45$. Being quantified as $\chi = 4\gamma/(1 - \alpha + \gamma) \times 100\%$ (see the Supporting Information for details), it varies in the $(Pb_{1-z}Sr_z)_{1-x}Fe_{1+x}O_{3-y}$ series from 48.9% ($z = 0.05$) to 49.5% ($z = 0.2$) and is equal to 50% in $(Pb_{1-z}Sr_z)_2Fe_2O_5$.

■ CONCLUSIONS

Stereochemically active lone-electron-pair cations are essential for the formation of CS planes in anion-deficient perovskites. In this study, we have demonstrated that these cations not only give rise to the CS planes but also largely influence their crystallographic orientation. Systematic investigation of the CS structures in the $(Pb_{1-z}Sr_z)_{1-x}Fe_{1+x}O_{3-y}$ perovskites reveals two distinct compositional ranges: $0.05 \leq z \leq 0.2$, where the CS plane orientation gradually varies but stays close to $(203)_p$, and $0.3 \leq z \leq 0.45$ with $(101)_p$ CS planes. Thus, upon a reduction in the amount of lone-pair cations, the $(203)_p$ CS structure transforms into the structure with the $(101)_p$ CS planes. Because charge and size differences between the Pb and Sr cations cannot be the factors governing the orientation of the CS planes, we relate this effect to the specific bonding of the Pb cations to the O atoms in these structures. For compounds with a high concentration of lone-pair cations, structures with the $(101)_p$ CS planes are not typical because of unfavorable bonding situations with competition of the lone-pair cations in the perovskite blocks for the 2p orbitals of the same O atoms. Besides, the orientation of the CS planes is affected by the decreasing flexibility of the perovskite blocks associated with the decreasing concentration of the lone-pair cations because the nonstereochemically active cations are prone to a symmetric coordination environment. We should note that a further decrease of the lone-pair cation concentration might again stabilize the CS planes with complex $(h0l)_p$ orientation. Indeed, the fraction of lone-pair cations involved in the formation of CS planes is lower for the $(h0l)_p$ CS planes than for the $(101)_p$ planes. However, the detailed structure would also depend on other factors, such as the oxidation state of the transition element, defining the separation between the adjacent CS planes.

■ ASSOCIATED CONTENT

Ⓢ Supporting Information

Crystallographic data of $Pb_{0.792}Sr_{0.168}Fe_{1.040}O_{2.529}$ in CIF format, EDX data of the compounds synthesized in this work, representative XRD patterns in each compositional range discussed, details on the construction of the (3 + 1)D occupational structural model of $(Pb_{1-z}Sr_z)_{1-x}Fe_{1+x}O_{3-y}$ ($0.05 \leq z \leq 0.2$), details on the Rietveld refinement of the $Pb_{0.792}Sr_{0.168}Fe_{1.040}O_{2.52}$ crystal structure, ED pattern of $Pb_{1.2}Sr_{0.8}Fe_2O_5$, magnetization curves of $Pb_{0.792}Sr_{0.168}Fe_{1.040}O_{2.529}$ and $Pb_{1.2}Sr_{0.8}FeO_5$ measured at 2 K, and parameters of the ^{57}Fe Mössbauer spectrum of $Pb_{0.792}Sr_{0.168}Fe_{1.040}O_{2.529}$. This material is available free of charge via the Internet at http://pubs.acs.org.

■ AUTHOR INFORMATION

Corresponding Author

*E-mail: Dmitry.Batuk@ua.ac.be. Phone: +32 3265 3305. Fax: +32 3265 3257.

Author Contributions

All authors have given approval to the final version of the manuscript.

Notes

The authors declare no competing financial interest.

■ ACKNOWLEDGMENTS

The authors are grateful to the Paul Scherrer Institute (PSI, Switzerland) for granting the beam time at the HRPT and to Denis Sheptyakov (PSI) for experimental support. M.B., D.B., and J.H. acknowledge funding from the Research Foundation Flanders (FWO) under Grant G.0184-09N. A.A.T. was partly supported by the Alexander von Humboldt Foundation and the Mobilitas grant of the ESF (Grant MTT77). We are grateful to Walter Schnelle (MPI CPfS) for his help with the high-temperature susceptibility measurements.

■ REFERENCES

(1) Anderson, J. S. In *Surface and Defect Properties of Solids*; Roberts, M. W., Thomas, J. M., Eds.; Royal Society of Chemistry: Cambridge, U.K., 1972; Vol. *1*, pp 1−53.

(2) Anderson, J. S.; Tilley, R. J. D. In *Surface and Defect Properties of Solids*; Roberts, M. W., Thomas, J. M., Eds.; Royal Society of Chemistry: Cambridge, U.K., 1974; Vol. 3, pp 1−56.

(3) Kosuge, K. *Chemistry of Non-stoichiometric Compounds*; Oxford University Press: Oxford, U.K., 1994; p 273.

(4) Ekström, T.; Tilley, R. J. D.; Watts, K. A. *J. Solid State Chem.* **1990**, *87*, 321−330.

(5) Ekström, T.; Iguchi, E.; Tilley, R. J. D. *J. Solid State Chem.* **1982**, *43*, 251−260.

(6) Allpress, J. G. *J. Solid State Chem.* **1972**, *4*, 173−185.

(7) Ekström, T.; Tilley, R. J. D. *J. Solid State Chem.* **1976**, *18*, 123−131.

(8) Andersson, S.; Collén, B.; Kuylenstierna, U.; Magnéli, A.; Pestmalis, H.; Åsbrink, S. *Acta Chem. Scand.* **1957**, *11*, 1641−1652.

(9) Horiuchi, H.; Tokonami, M.; Morimoto, N.; Nagasawa, K.; Bando, Y.; Takada, T. *Mater. Res. Bull.* **1971**, *6*, 833−843.

(10) Magnéli, A. *Acta Crystallogr.* **1953**, *6*, 495−500.

(11) Gadó, P.; Holmberg, B.; Magnéli, A.; Kallner, A. *Acta Chem. Scand.* **1965**, *19*, 2010−2011.

(12) Tilley, R. J. D. *J. Solid State Chem.* **1976**, *19*, 53−62.

(13) Iguchi, E.; Tilley, R. J. D. *Philos. Trans. R. Soc., A* **1977**, *286*, 55−85.

(14) Iguchi, E.; Tilley, R. J. D. *J. Solid State Chem.* **1978**, *24*, 131−141.

(15) Mitchell, R. H. *Perovskites: Modern and Ancient*; Almaz Press Inc.: Ontario, Canada, 2002; p 316.

(16) Abakumov, A. M.; Hadermann, J.; Bals, S.; Nikolaev, I. V; Antipov, E. V.; Van Tendeloo, G. *Angew. Chem., Int. Ed.* **2006**, *45*, 6697−6700.

(17) Abakumov, A. M.; Hadermann, J.; Van Tendeloo, G.; Antipov, E. V. *J. Am. Ceram. Soc.* **2008**, *91*, 1807−1813.

(18) Abakumov, A. M.; Batuk, D.; Hadermann, J.; Rozova, M. G.; Sheptyakov, D. V.; Tsirlin, A. A.; Niermann, D.; Waschkowski, F.; Hemberger, J.; Van Tendeloo, G.; Antipov, E. V. *Chem. Mater.* **2011**, *23*, 255−265.

(19) Grenier, J. C.; Pouchard, M.; Hagenmuller, P. *Rev. Chim. Miner.* **1977**, *14*, 515−522.

(20) Catalan, G.; Scott, J. F. *Adv. Mater.* **2009**, *21*, 2463−2485.

(21) Abakumov, A. M.; Hadermann, J.; Batuk, M.; D'Hondt, H.; Tyablikov, O. A.; Rozova, M. G.; Pokholok, K. V.; Filimonov, D. S.; Sheptyakov, D. V.; Tsirlin, A. A.; Niermann, D.; Hemberger, J.; Van Tendeloo, G.; Antipov, E. V. *Inorg. Chem.* **2010**, *49*, 9508−9516.

(22) Abakumov, A. M.; Batuk, M.; Tsirlin, A. A.; Tyablikov, O. A.; Sheptyakov, D. V.; Filimonov, D. S.; Pokholok, K. V.; Zhidal, V. S.; Rozova, M. G.; Antipov, E. V.; Hadermann, J.; Van Tendeloo, G. *Inorg. Chem.* **2013**, *52*, 7834−7843.

(23) Shannon, R. D. *Acta Crystallogr., Sect. A* **1976**, *32*, 751−767.
(24) Fischer, P.; Frey, G.; Koch, M.; Könnecke, M.; Pomjakushin, V.; Schefer, J.; Thut, R.; Schlumpf, N.; Bürge, R.; Greuter, U.; Bondt, S.; Berruyer, E. *Phys. B: Condens. Matter* **2000**, *276−278*, 146−147.
(25) Petricek, V.; Dusek, M.; Palatinus, L. *JANA2006. The crystallographic computing system*; Institute of Physics, Praha, Czech Republic, 2006.
(26) Prescher, C.; McCammon, C.; Dubrovinsky, L. *J. Appl. Crystallogr.* **2012**, *45*, 329−331.
(27) Hadermann, J.; Abakumov, A. M.; Nikolaev, I. V.; Antipov, E. V.; Van Tendeloo, G. *Solid State Sci.* **2008**, *10*, 382−389.
(28) Raynova-Schwarten, V.; Massa, W.; Babel, D. *Z. Anorg. Allg. Chem.* **1997**, *623*, 1048−1054.
(29) Lepoittevin, C.; Hadermann, J.; Malo, S.; Pérez, O.; Van Tendeloo, G.; Hervieu, M. *Inorg. Chem.* **2009**, *48*, 8257−8262.
(30) Van Smaalen, S. *Incommensurate Crystallography*; Oxford University Press: Oxford, U.K., 2007.
(31) Janssen, T.; Janner, A.; Looijenga-Vos, A.; de Wolff, P. M. *International Tables for Crystallography*; Springer: New York, 2006; pp 907−955.
(32) Hartel, P.; Rose, H.; Dinges, C. *Ultramicroscopy* **1996**, *63*, 93−114.
(33) Petříček, V.; van der Lee, A.; Evain, M. *Acta Crystallogr., Sect. A* **1995**, *51*, 529−535.
(34) Nikolaev, I.; D’Hondt, H.; Abakumov, A. M.; Hadermann, J.; Balagurov, A. M.; Bobrikov, I.; Sheptyakov, D.; Pomjakushin, V.; Pokholok, K.; Filimonov, D.; Van Tendeloo, G.; Antipov, E. V. *Phys. Rev. B* **2008**, *78*, 024426.
(35) Menil, F. *J. Phys. Chem. Solids* **1985**, *46*, 763−789.
(36) Smit, J.; Wijn, H. P. J. *Ferrites*; Philips’ Technical Library: Eindhoven, The Netherlands, 1959; p 384.
(37) Brown, I. D.; Shannon, R. D. *Acta Crystallogr., Sect. A* **1973**, *29*, 266−282.
(38) Nelmes, R. J.; Kuhs, W. F. *Solid State Commun.* **1985**, *54*, 721−723.
(39) Walsh, A.; Payne, D. J.; Egdell, R. G.; Watson, G. W. *Chem. Soc. Rev.* **2011**, *40*, 4455−4463.
(40) Tzvetkov, P.; Petrova, N.; Kovacheva, D. *J. Alloys Compd.* **2009**, *485*, 862−866.